RAA 2019 Vol. **19** No. **7**, 98(16pp) doi: 10.1088/1674–4527/19/7/98
© 2019 National Astronomical Observatories, CAS and IOP Publishing Ltd.
http://www.raa-journal.org *http://iopscience.iop.org/raa*

***R**esearch in*
***A**stronomy and*
***A**strophysics*

X-ray activity from different types of stars

Lin He[1,2], Song Wang[2], Xiao-Jie Xu[1], Roberto Soria[3,4,5], Ji-Feng Liu[2,3,6], Xiang-Dong Li[1], Yu Bai[2], Zhong-Rui Bai[2], Jin-Cheng Guo[7,⋆], Yan-Li Qiu[2,3], Yong Zhang[8], Ruo-Chuan Xu[9], and Ke-Cheng Qian[10]

[1] School of Astronomy and Space Science and Key Laboratory of Modern Astronomy and Astrophysics, Nanjing University, Nanjing 210093, China
[2] Key Laboratory of Optical Astronomy, National Astronomical Observatories, Chinese Academy of Sciences, Beijing 100101, China; *songw@bao.ac.cn*
[3] College of Astronomy and Space Sciences, University of Chinese Academy of Sciences, Beijing 100049, China
[4] International Centre for Radio Astronomy Research, Curtin University, GPO Box U1987, Perth, WA 6845, Australia
[5] Sydney Institute for Astronomy, School of Physics A28, The University of Sydney, Sydney, NSW 2006, Australia
[6] WHU-NAOC Joint Center for Astronomy, Wuhan University, Wuhan 430072, China
[7] Department of Astronomy, Peking University, Beijing 100871, China
[8] Nanjing Institute of Astronomical Optics & Technology, National Astronomical Observatories, Chinese Academy of Sciences, Nanjing 210042, China
[9] International Department, the Affiliated High School of SCNU, Guangzhou 510630, China
[10] United World College, Changshu 215500, China

Received 2018 September 17; accepted 2019 February 3

Abstract X-ray emission is an important indicator of stellar activity. In this paper, we study stellar X-ray activity using the *XMM-Newton* and LAMOST data for different types of stars. We provide a sample including 1259 X-ray-emitting stars, of which 1090 have accurate stellar parameter estimations. Our sample size is much larger than those used in previous works. We find a bimodal distribution of the X-ray to optical flux ratio ($\log(f_{\rm X}/f_V)$) for G and K stars. We interpret that this bimodality is due to two subpopulations with different coronal heating rates. Furthermore, using the full widths at half maxima calculated from Hα and Hβ lines, we show that these stars in the inactive peaks have smaller rotational velocities. This is consistent with the magnetic dynamo theory that presumes stars with low rotational velocities have low levels of stellar activity. We also examine the correlation between $\log(f_{\rm X}/f_V)$ and luminosity of the excess emission in the Hα line, and find a tight relation between the coronal and chromospheric activity indicators.

Key words: X-rays: stars — stars: activity — stars: late-type

1 INTRODUCTION

Stars of almost all stellar classes are X-ray emitters (Harnden et al. 1979; Stocke et al. 1983; Schmitt et al. 1995; Rogel et al. 2006). X-ray emission from late-type main-sequence stars comes from a magnetic corona which contains plasma at a temperature exceeding ∼1 million K. The coronal magnetic structures and heating mechanisms are controlled by surface magnetic fields (Güdel 2004), with the latter generally thought to be caused by a complex dynamo mechanism (e.g., Pizzolato et al. 2003).

The magnetic dynamo mechanism has been observationally evidenced by the famous activity-rotation correlation (Skumanich 1972). Walter & Bowyer (1981) discovered the relation between X-ray luminosity ($L_{\rm X}$) and rotation for RS CVn systems. A more accurate relation, $L_{\rm X} \sim 10^{27}(V \sin i)^2$, was given by Pallavicini et al. (1981) for late-type stars. Furthermore, it was found that the activity-rotation correlation depends on the stellar mass (Pizzolato et al. 2003). This is explained by the fact that the generation of magnetic energy by large-scale dynamo action is driven by rotation and convection (e.g., Charbonneau 2010; Reiners et al. 2014). On the other hand, there is

⋆ LAMOST Fellow

a saturated X-ray luminosity ($L_{\rm X}/L_{\rm bol} \approx 10^{-3}$, where $L_{\rm bol}$ is the bolometric luminosity) for most active stars where $L_{\rm X}/L_{\rm bol}$ does not change below a certain rotation period (Vilhu 1984; Vilhu & Walter 1987). Two scenarios are often implemented to explain the saturation and super-saturation (i.e., the activity starts decreasing as the stellar rotation rate increases to a critical value; Prosser et al. 1996) of stellar activity: polar up-drift migration (Solanki et al. 1997) and centrifugal stripping (Jardine & Unruh 1999).

Although there have been many studies on stellar X-ray emission, some issues are still poorly understood, such as coronal heating and the evolution of stellar activity. One main limitation of previous studies is the small sample size of X-ray emitting stars with accurate stellar parameter estimations. This paper uses the largest spectral database, from observations by the Large Sky Area Multi-object Fiber Spectroscopic Telescope (LAMOST, also known as the Guo Shou Jing Telescope), to present stellar parameters (e.g., effective temperature, surface gravity and metallicity) for more than 1200 X-ray emitting stars observed by *XMM-Newton*. We will study stellar X-ray activities over a wide range of stellar parameters. This may help us improve our understanding of these open issues (Testa et al. 2015).

The paper is organized as follows. In Section 2, we show the data analysis and sample selection from the 3XMM-DR5 (Rosen et al. 2016) and the LAMOST DR3 (Luo et al. 2015). In Section 3, we calculate the X-ray to optical flux ratio, and study the correlation between the X-ray to optical flux ratio and different stellar parameters. In Section 4, we discuss and explain the bimodality of stellar X-ray activity. Finally, we summarize the results in Section 5.

2 SAMPLE SELECTION AND DATA REDUCTION

2.1 Sample Selection

We cross-matched the 3XMM-DR5 catalog and the LAMOST DR3 catalog using a radius of $3''$. This led to 3579 unique *XMM-Newton* sources with LAMOST spectral observations. To calculate the likelihood of mismatch, we shifted the positions of the *XMM-Newton* sources by $1'$, and cross-matched them with the LAMOST catalog again using the same radius. In this case, we obtained 135 matches, and we conclude that the likelihood of mismatch is about 3.77%.

We applied several criteria to get a clean sample. Firstly, for the *XMM-Newton* data, we selected sources with SUM_FLAG ≤ 2 and SC_EXTENT $= 0$. The former is the summary flag derived from the EPIC warning flags, which is implemented to exclude spurious detections; the latter is the total band extent that is utilized to recognize point sources. Secondly, for the LAMOST spectra, we only used those with signal-to-noise ratio (SNR) higher than 7.5 in the r band. Thirdly, there are four main classes in the LAMOST database: "STAR", "GALAXY", "QSO" and "Unknown". Spectra flagged as "Unknown" were excluded from the sample. Some other sources, like double stars and white dwarfs, were also discarded according to the classification of the LAMOST catalog. This led to a sample of 1564 sources, including 134 galaxies, 60 quasi-stellar objects (QSOs) and 1370 stars. Finally, we cross-matched the 1370 stars with the SIMBAD database using a radius of $3''$. About 100 sources are actually not main-sequence stars: 59 multiple objects, 32 pre-main-sequence stars, 18 globular clusters, one galaxy and one possible active galactic nucleus (AGN). All these sources were excluded from the stellar sample. We visually checked all the spectra of the sample sources (e.g., stars, galaxies and QSOs), and the final stellar sample contains 1259 stars.

2.2 LAMOST Data

LAMOST is a reflecting Schmidt telescope with a clear aperture of 4 meters and a field of view of 5 degrees (Cui et al. 2012; Zhao et al. 2012). With 4000 fibers, it started its optical spectroscopic survey in 2012, and has successfully accomplished the fourth year mission (Deng et al. 2012; Luo et al. 2015). The third data release, DR3, contains 5 755 126 spectra, including 5 268 687 stellar spectra, 61 815 galaxy spectra, 16 351 spectra of QSOs and 408 273 spectra of unknown objects (Luo et al. 2015). In this work, we obtained the effective temperature ($T_{\rm eff}$), metallicity ([Fe/H]) and surface gravity ($\log(g)$) from the stellar parameter catalogs for A-, F-, G- and K-type stars. Typical uncertainties of the $T_{\rm eff}$ and $\log(g)$ are about 150 K and 0.3 dex (Wu et al. 2011) respectively.

We collected the extinction estimations from Xiang et al. (2017); the typical uncertainty of $E(B-V)$ in their catalog is about 0.03. Finally, we calculated the equivalent width (EW) of the Hα line, and the full width at half maximum (FWHM) of Hα and Hβ lines. The EW is calculated using the following formula

$$\mathrm{EW} = \int \frac{f(\lambda) - f(0)}{f(0)} d\lambda \ , \qquad (1)$$

where $f(0)$ denotes the nearby pseudo-continuum flux.

2.3 *XMM-Newton* Data

The 3XMM-DR5 catalog (Rosen et al. 2016) contains 565 962 X-ray detections comprising 396 910 unique X-ray sources, which is one of the largest X-ray source catalogs ever produced. We used PIMMS[1] to convert the 0.2–12 keV count rate (CR) to the unabsorbed 0.3–3.5 keV flux for the PN, M1 and M2. For stars, we assumed an APEC model with individual absorptions, solar abundance and a moderate coronal temperature ($\log T = 6.5$) (Schmitt et al. 1990). The individual absorptions for stars were converted from their extinctions (Foight et al. 2016),

$$N_{\rm H} = (2.87 \pm 0.12) \times 10^{21} A_V \ {\rm cm}^{-2} \ . \qquad (2)$$

The uncertainty of $N_{\rm H}$ is about $2.67 \times 10^{20}\,{\rm cm}^{-2}$. We should note that the unabsorbed X-ray flux $f_{\rm X}$, converted from the CR using PIMMS, is dependent on the coronal temperature set in the APEC model. However, the exact plasma temperature is not accurately known. To evaluate the influence on $f_{\rm X}$, we re-estimated it with a higher temperature ($\log T = 7$). Using the mean value of $N_{\rm H}$ ($\approx 10^{21}\,{\rm cm}^{-2}$) for the sample stars, we find $f_{\rm X}$ decreases by a factor of ≈ 0.05. Therefore, the influence of plasma temperature can be ignored in our study.

For galaxies and QSOs, we assumed a power-law model with $\Gamma = 1.7$ and Galactic foreground absorptions (Schlafly & Finkbeiner 2011). Then, we obtained $f_{\rm X}$ as the mean value of the three cameras weighted by the errors. We used the EP_HR2 as the hardness ratio (HR), which is defined as $({\rm CR}_{1-2\ {\rm keV}} - {\rm CR}_{0.5-1\ {\rm keV}})/({\rm CR}_{1-2\ {\rm keV}} + {\rm CR}_{0.5-1\ {\rm keV}})$ and calculated by averaging over all three cameras.

3 RESULTS

3.1 X-ray to Optical Flux Ratio

The ranges of the X-ray to optical flux ratio are distinctly different for each stellar type, AGNs, BL Lac objects, clusters of galaxies and normal galaxies (e.g., Stocke et al. 1991; Hornschemeier et al. 2003; Zickgraf et al. 2003; Brusa et al. 2007; Luo et al. 2008). Using the definition from Maccacaro et al. (1988), we estimated $\log(f_{\rm X}/f_V)$ as

$$\log(f_{\rm X}/f_V) = \log(f_{\rm X}) + 0.4V_0 + 5.37 \ , \qquad (3)$$

where $f_{\rm X}$ is the unabsorbed 0.3–3.5 keV flux and V_0 is the extinction-corrected V-band magnitude.

[1] *https://heasarc.gsfc.nasa.gov/docs/software/tools/pimms.html*

In order to obtain the V-band magnitude, we cross-matched the LAMOST DR3 catalog and the UCAC4 catalog (Zacharias et al. 2013) with a radius of $3''$. For objects without a UCAC4 V-band magnitude, we calculated it using the g and r magnitudes from the Sloan Digital Sky Survey (SDSS) following Jester et al. (2005)

$$V_0 = g_0 - 0.59 \times (g-r)_0 - 0.01 \ . \qquad (4)$$

The errors of $\log(f_{\rm X}/f_V)$ were calculated as a combination of the errors of X-ray flux, V-band magnitude and extinction. The X-ray information and the stellar parameters from the LAMOST catalog are summarized in Tables 1 and 2 respectively.

3.2 $\log(f_{\rm X}/f_V)$ for Stellar and Non-stellar Objects

Different kinds of objects have their typical ranges of $\log(f_{\rm X}/f_V)$ values (Fig. 1). Most of the stars have $\log(f_{\rm X}/f_V)$ less than -1; most of the galaxies have $\log(f_{\rm X}/f_V)$ between -3 and -1, and most of the QSOs have $\log(f_{\rm X}/f_V)$ between -1 and $+1$. These ranges are consistent with previous works (e.g., Stocke et al. 1991; Krautter et al. 1999; Georgakakis et al. 2004; Agüeros et al. 2009).

For the stellar sample, we divided these stars into four groups according to their spectral types. Each stellar type shows the widest range of emission levels, with $\log(f_{\rm X}/f_V)$ ranging from ≈ -5 to ≈ -1 (Fig. 2). Generally, late-type stars have a higher $\log(f_{\rm X}/f_V)$ than early-type stars, because the optical luminosity decreases more rapidly than the X-ray luminosity for decreasing stellar masses. The distributions of G and K stars exhibit bimodality, which is consistent with previous studies (Stocke et al. 1991; Agüeros et al. 2009; Lin et al. 2012). For G stars, there are more inactive stars than active ones, while for K stars, more active stars are apparent. The $\log(f_{\rm X}/f_V)$ distributions of K subtypes display clear bimodality (Fig. 3). However, due to the sample limit, it is difficult to claim whether the G subtypes manifest bimodal distributions or broad distributions with local peaks. A clear evolutionary trend of the X-ray activity can be seen: from a single inactive distribution (F type), to a weak bimodal distribution (G type), to a clear bimodal distribution (K type), to a single active distribution (M type). Future work with a larger sample may shed more light on distributions of the subtypes.

3.3 Comparison with Previous Works

Agüeros et al. (2009) calculated $\log(f_{\rm X}/f_V)$ for 317 stars using the ROSAT All-Sky Survey (RASS; Voges et al.

Table 1 The X-ray Information for the Sample Sources

Obsid	$f_{\rm X}$ (erg s^{-1} cm^{-2})	$\log(f_{\rm X}/f_V)$	HR
(1)	(2)	(3)	(4)
1603040	9.67e–15±1.71e–15	–2.51±0.14	0.57±1.11
7003074	5.06e–14±4.81e–15	–1.93±0.06	0.23±0.44
7003243	5.11e–15±6.01e–16	–2.78±0.07	–1.00±2.41
7711046	3.72e–14±3.63e–15	–2.14±0.06	–1.00±0.35
20001189	5.74e–14±1.86e–15	–1.49±0.04	–0.36±0.06
28306100	5.44e–15±8.75e–16	–3.89±0.08	–0.89±1.00
51007061	1.68e–14±1.37e–15	–3.80±0.05	–1.00±0.90
53111238	2.26e–14±2.53e–15	–4.12±0.06	–0.93±1.66
74309103	1.69e–14±1.78e–15	–4.61±0.09	–1.00±0.53
74311158	3.54e–14±2.38e–15	–4.19±0.08	–0.91±0.43
74403036	1.74e–14±1.10e–15	–3.64±0.05	–0.55±0.29
75805212	3.10e–14±1.48e–15	–2.42±0.05	–0.69±0.13
76406132	2.17e–14±2.01e–15	–4.43±0.05	–0.82±0.40
76506084	1.29e–14±1.32e–15	–3.59±0.06	–0.95±0.62
84812137	2.92e–14±2.97e–15	–3.53±0.06	–0.74±0.94

Notes: Column (1): spectral ID in LAMOST catalog. Col. (2): unabsorbed flux in band 0.3–3.5 keV. Col. (3): X-ray to optical flux ratio. Col. (4): EPIC HR using the bands of 0.5–1 keV and 1–2 keV derived from the 3XMM-DR5 catalog. This entire table is available at *http://www.raa-journal.org/docs/Supp/ms4332Table1.txt*.

Table 2 Stellar Parameters for the Sample Sources

Obsid	RA (deg)	DEC (deg)	Subclass	V (mag)	A_V (mag)	$N_{\rm H}$ (cm^{-2})	$T_{\rm eff}$ (K)	$\log(g)$	[Fe/H]
(1)	(2)	(3)	(4)	(5)	(6)	(7)	(8)	(9)	(10)
1603040	9.873834	40.083248	G9	15.77±0.29	0.38	1.09e+21	5020.89±211.08	4.27±0.63	0.09±0.28
1615104	11.123160	41.359930	K1	14.17±0.03	1.12	3.22e+21	4808.98±106.97	3.05±0.58	-0.58±0.16
1615179	10.716530	41.518950	F6	15.81±0.01	1.31	3.77e+21	5280.53±322.29	3.04±1.17	-1.42±0.52
1615187	10.939620	41.616010	K3	15.34±0.08	0.64	1.82e+21	4872.15±256.63	3.42±0.61	-0.24±0.33
7003074	9.322592	40.763245	K5	15.25±0.05	0.23	6.54e+20	4491.66±88.32	4.22±0.26	-0.14±0.13
7003243	9.630176	40.286594	G8	15.70±0.07	0.30	8.58e+20	5141.44±194.22	4.08±0.54	-0.07±0.24
7711046	16.773656	32.182487	K5	15.02±0.05	0.19	5.32e+20	4464.46±121.34	4.01±0.30	0.10±0.16
20001189	185.349817	28.070038	K3	16.15±0.01	0.17	4.74e+20	4809.03±154.27	4.64±0.27	-0.04±0.23
28114180	98.454761	17.791983	G5	11.83±0.03	0.68	1.96e+21	5094.17±114.29	2.73±0.59	0.01±0.16
28306100	139.828255	30.428329	G3	12.63±0.05	0.07	2.09e+20	5728.46±166.85	4.41±0.52	-0.10±0.18
42815236	98.925573	5.526181	K0	11.61±0.14	0.89	2.55e+21	4745.80±54.52	2.69±0.52	-0.39±0.09
43810009	98.397596	17.657734	K4	14.40±0.04	1.88	5.38e+21	4599.58±120.03	1.82±0.57	-0.66±0.20
51007061	239.800512	27.268972	G3	11.75±0.01	0.20	5.81e+20	5821.85±122.08	4.06±0.56	0.06±0.13
53111238	235.942430	54.151718	F6	10.58±0.04	0.16	4.57e+20	6404.79±121.72	4.19±0.42	0.03±0.12
74309103	35.130959	-6.186942	F0	9.61±0.17	0.09	2.47e+20	6750.24±182.92	4.13±0.38	-0.04±0.18

Notes: Column (1): spectral ID in LAMOST catalog. Col. (2): right ascension. Col. (3): declination. Col. (4): stellar subclass. Col. (5): V-band magnitude. Col. (6): extinction in the V band. Col. (7): hydrogen column density converted from optical extinction. Col. (8): effective temperature. Col. (9): surface gravity. Col. (10): metallicity. This entire table is available at *http://www.raa-journal.org/docs/Supp/ms4332Table2.txt*.

1999) and SDSS catalogs. Figure 4 shows a comparison of the $\log(f_{\rm X}/f_V)$ distribution between Agüeros et al. (2009) and our work. There are 124, 110, 67 and 15 stars in the F, G, K and M types from Agüeros et al. (2009), respectively. In our work, there are two B stars, 36 A stars, 317 F stars, 405 G stars, 332 K stars and 167 M stars.

Generally, the $\log(f_{\rm X}/f_V)$ distributions of each spectral type in the two works are in good agreement. However, the distribution of K type stars in our sample displays a more obvious double-peak structure than that of Agüeros et al. (2009). There are much less active K stars in Agüeros et al. (2009). This could be due to the energy limit (0.2–2.4 keV) of the *ROSAT* mission, which means that Agüeros et al. (2009) may have lost some of the sources with harder spectra that have higher $\log(f_{\rm X}/f_V)$ values (Sect. 4.2). On the other hand, there are more inactive M stars in our sam-

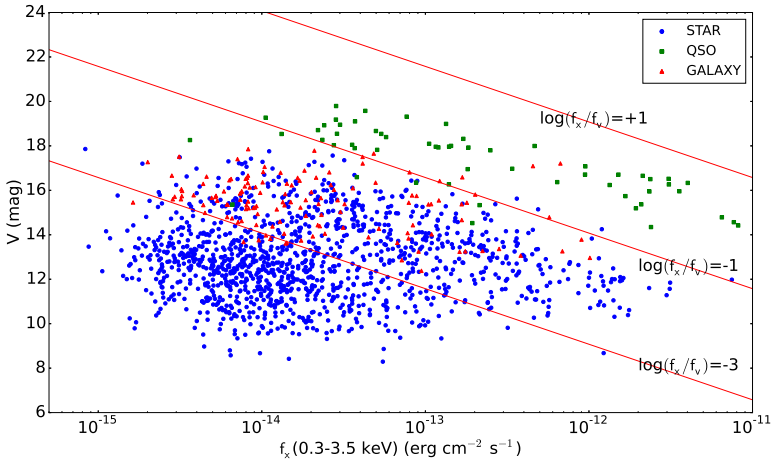

Fig. 1 V magnitude against $f_{\rm X}$ (0.3–3.5 keV). The *blue*, *green* and *red points* indicate stars, QSOs and galaxies that are classified by the LAMOST catalog respectively. The *red lines* signify constant X-ray to optical flux ratios as $+1$, -1 and -3.

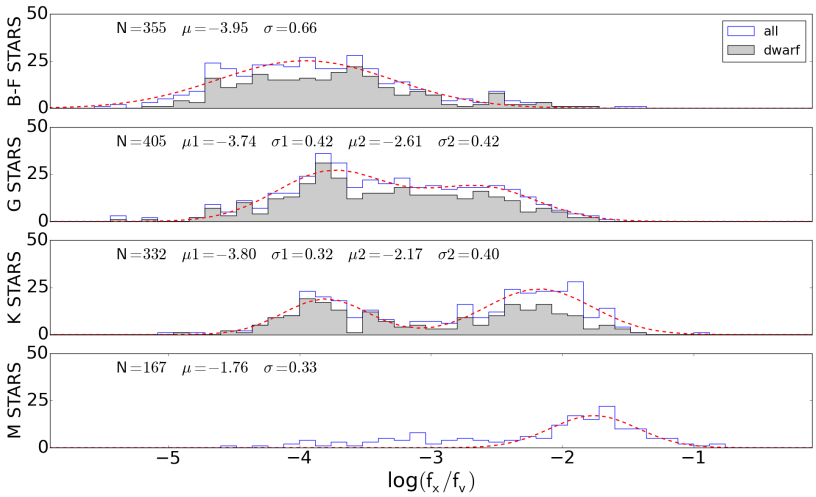

Fig. 2 $\log(f_{\rm X}/f_V)$ distributions for B, A, F, G, K and M stars. The B, A and F groups are shown in one panel due to the small number of stars. The *red dashed lines* are the Gaussian fittings to the histograms. For the B–F and M groups, single-Gaussian functions are used for the fitting, while for the G and K groups, double-Gaussian functions are used to fit the $\log(f_{\rm X}/f_V)$ distributions. N, μ and σ indicate the number of sources, mean value and standard deviation respectively. *Gray histograms* represent the dwarfs in each spectral type. For B and M stars, no $\log(g)$ value was given by the LAMOST catalog, thus no giant or dwarf classification was done for them.

ple. We propose that this is due to a higher sensitivity of the *XMM-Newton* mission, and therefore more sources with lower $\log(f_{\rm X}/f_V)$ values can be detected.

3.4 Correlation Between $\log(f_{\rm X}/f_V)$ and Stellar Parameters

Using stellar parameter estimations from LAMOST, we study the correlations between $\log(f_{\rm X}/f_V)$ and stellar properties, including $T_{\rm eff}$, $\log(g)$, [Fe/H] and Hα emission.

3.4.1 $\log(f_{\rm X}/f_V)$ *vs.* $T_{\rm eff}$ *and* $\log(g)$

The bimodality of G- and K-type stars can also be seen in the $\log(f_{\rm X}/f_V)$–$T_{\rm eff}$ diagram (Fig. 5). We divided the sources into two branches. For the primary branch, which contains the main part of the sources (outside the dashed rectangle), $\log(f_{\rm X}/f_V)$ decreases with increasing temperature. This result is compatible with previous works (Stocke et al. 1991; Agüeros et al. 2009). For the secondary branch (inside the blue dashed box), stars generally have constant low $\log(f_{\rm X}/f_V)$ values for varying effective temperatures. The secondary branch is mainly constructed from cool stars ($T_{\rm eff} < 5800$ K). We roughly defined a region for the secondary branch in the stellar parameter space: $3800\,{\rm K} < T_{\rm eff} \leq 5800\,{\rm K}$; $-4.2 < \log(f_{\rm X}/f_V) \leq -3.3$; $4.5 < \log(g) \leq 4.9$. The constraint on $\log(g)$ aims to exclude giant stars. The secondary branch contains most of the inactive G- and K-type stars, and it can be re-

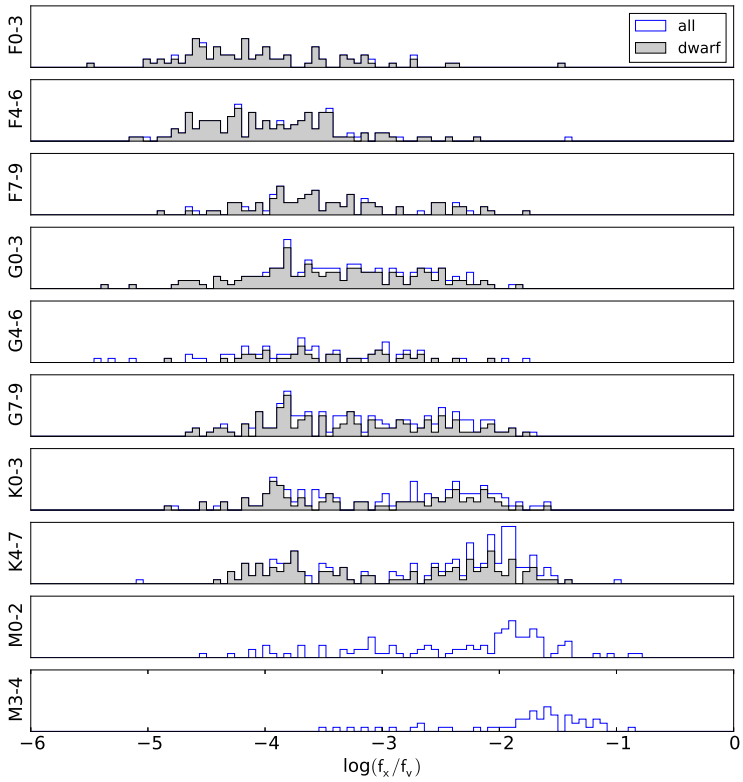

Fig. 3 $\log(f_{\rm X}/f_V)$ distributions for subtypes of the F, G, K and M stars. *Gray histograms* represent the dwarfs in each spectral type. For M stars, no $\log(g)$ value was given by the LAMOST catalog, thus no giant or dwarf classification was done for them.

garded as the inactive part of the two types of stars. On the other hand, a group of stars (3800 K $< T_{\rm eff} <$5800 K; $\log(f_{\rm X}/f_V) > -3.3$) in the primary branch can be considered as the active part of the G and K stars.

There are $\approx$ 108 giants showing X-ray emission, and some have high X-ray activity (Fig. 6). This is consistent with previous studies that indicate late-type giants can manifest (high) stellar activity (Simon & Drake 1989; Aurière et al. 2015). However, some giants or sub-giants exhibiting stellar activity may be in unrecognized binary systems (Özdarcan & Dal 2018), and our data are not sufficient to associate the X-ray emission with the giants themselves or their unresolved dwarf companions (Schröder & Schmitt 2007).

3.4.2 $\log(f_{\rm X}/f_V)$ *vs. [Fe/H]*

There is no clear evidence for a correlation between X-ray activity and metallicity (Fig. 7), however, for active stars ($\log(f_{\rm X}/f_V) > -3$), a weak correlation between $\log(f_{\rm X}/f_V)$ and [Fe/H] is seen: more active stars are more metal-poor. This is consistent with Rocha-Pinto & Maciel (1998), where it is reported that the metallicities of very active stars are lower than those of normally active stars. Those inactive stars in the secondary branch are generally more metal-rich than the active stars (of the same spectral type) in the primary branch (Fig. 8).

3.4.3 $\log(f_{\rm X}/f_V)$ *vs. H*α *emission*

Both X-ray and Hα emission are proxies of stellar magnetic activity (Testa et al. 2015), although they exist at different layers of a stellar atmosphere (i.e., corona and chromosphere respectively). LAMOST in combination with *XMM-Newton* provides us with a great opportunity to study the relation between the two activity indicators. The EWs of Hα lines are listed in Table 3. Stars with a positive EW, which means Hα emission line, have higher $\log(f_{\rm X}/f_V)$ values (Fig. 9). All stars in the secondary branch (i.e., X-ray inactive) and most of the stars in the primary branch, which have low $\log(f_{\rm X}/f_V)$ values, do not have Hα excess emissions. As an example, the LAMOST spectra for two stars (one active and one inactive) are shown in Figure 10.

However, the EW is not a suitable indicator of stellar activity since the continuum flux is very sensitive to the effective temperature (Reid et al. 1995; Yang et al. 2017). To remove the effects of effective temperature and surface gravity, we used the ratio of Hα excess flux and bolomet-

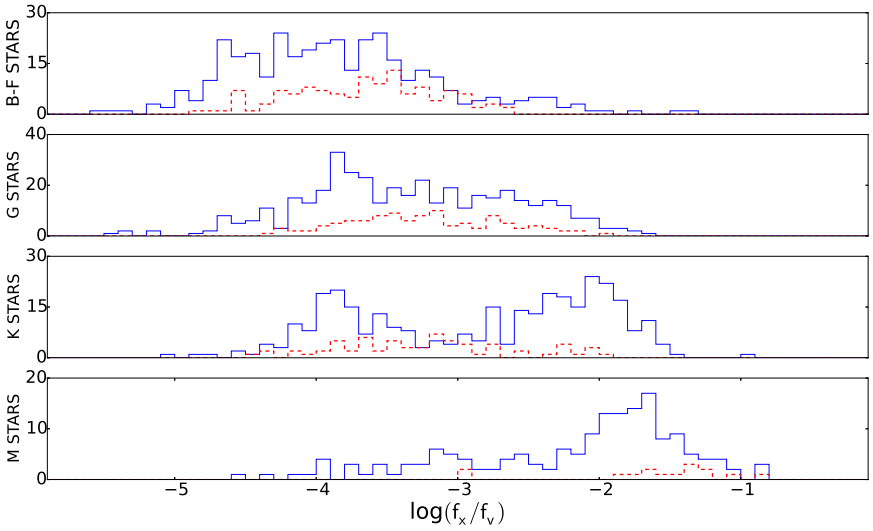

Fig. 4 Comparison of $\log(f_{\rm X}/f_V)$ distributions for each spectral type in our sample and in Agüeros et al. (2009). The *red dashed histograms* represent the sample from Agüeros et al. (2009), including 124, 110, 67 and 15 stars of the spectral types F, G, K and M, respectively. The *blue histograms* correspond to the distributions of our sample, including two B stars, 36 A stars, 317 F stars, 405 G stars, 332 K stars and 167 M stars.

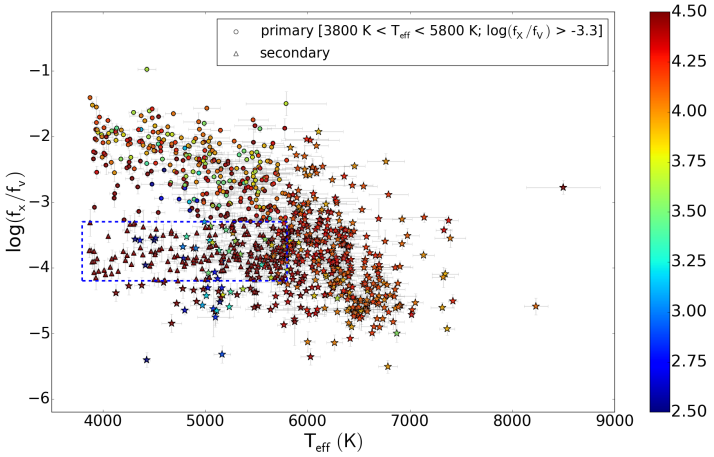

Fig. 5 $\log(f_{\rm X}/f_V)$ as a function of temperature. The color signifies different levels of $\log(g)$. The *triangles* inside the *dashed rectangle* mark the sources of the secondary branch. The *circles* represent the active part of the G and K stars in the primary branch, while the *pentagrams* represent the other part of the primary branch.

ric flux to describe the activity of the chromosphere. First, we constructed a "base line" of Hα emissions using the inactive stars in the secondary branch (Fig. 11). The excess EW (hereafter EW′) is calculated by subtracting the base value at the same temperature, i.e.,

$$\mathrm{EW}' = \mathrm{EW} - \mathrm{EW}_{\rm base}\ . \tag{5}$$

Then, we calculated the stellar surface fluxes of the Hα emission lines ($f_{\rm H\alpha}$) using the stellar atmosphere model CK04 (Castelli & Kurucz 2004) based on the EW′. The CK04 models list physical fluxes of the spectra in units of erg cm^{-2} s^{-1} A^{-1}. For each star, the model with the most similar $T_{\rm eff}$, $\log(g)$ and [Fe/H] was used. Finally, we determined the flux ratio $f_{\rm H\alpha}/f_{\rm bol}$ using the bolometric flux $f_{\rm bol} = \sigma\, T^4$, with the stellar temperature from LAMOST. A power-law dependence of $f_{\rm X}/f_V$ on $f_{\rm H\alpha}/f_{\rm bol}$ (Fig. 12) is determined as,

$$\begin{aligned}\log(f_{\rm X}/f_V) =&(1.21 \pm 0.23) \times \log(f_{\rm H\alpha}/f_{\rm bol}) \\ &+ (2.53 \pm 0.87)\ .\end{aligned} \tag{6}$$

Recently, Martínez-Arnáiz et al. (2011) reported a relation between X-ray and Hα emission as $F_{\rm X} \propto F_{\rm H\alpha}^{1.48\pm0.07}$, using a sample of late-type dwarf active stars with spectral types from F to M. For M dwarfs, Stelzer

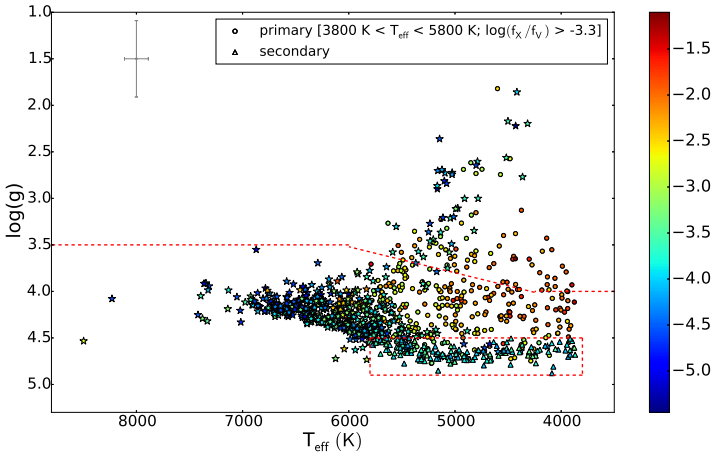

Fig. 6 $\log(g)$ as a function of temperature. The color signifies different levels of $\log(f_{\rm X}/f_V)$. The *red dashed line* is the separation between giant and dwarf stars (Ciardi et al. 2011). The meanings of the symbols are the same as in Fig. 5.

Table 3 Estimated Parameters for the Hα and Hβ Lines

Obsid	Subclass	$\mathrm{EW_{H\alpha}}$ (Å)	$\mathrm{EW'_{H\alpha}}$ (Å)	$\log(f_{\rm H\alpha}/f_{\rm bol})$	$\mathrm{FWHM_{H_\beta,cor}}$ (Å)	$\mathrm{FWHM_{H_\alpha,cor}}$ (Å)
(1)	(2)	(3)	(4)	(5)	(6)	(7)
1603040	G9	–0.44 ± 0.04	...	...	...	...
1615104	K1	–0.61 ± 0.03	...	...	...	...
1615179	F6	–1.67 ± 0.08	...	...	...	...
1615187	K3	–0.45 ± 0.45	...	...	...	...
7003074	K5	1.30 ± 0.22	1.93	–3.73 ± 0.05	...	1.26 ± 2.66
7003243	G8	–0.48 ± 0.06	...	...	3.42 ± 5.03	...
7711046	K5	0.78 ± 0.13	...	...	...	...
20001189	K3	–0.88 ± 0.12	...	...	...	...
28114180	G5	–1.31 ± 0.03	...	...	...	...
28306100	G3	–1.97 ± 0.04	...	...	1.84 ± 1.53	...
42815236	K0	–0.72 ± 0.03	...	...	...	...
43810009	K4	–0.81 ± 0.03	...	...	...	...
51007061	G3	–2.17 ± 0.05	...	...	2.28 ± 1.11	2.29 ± 1.07
53111238	F6	–2.56 ± 0.06	...	...	...	3.23 ± 0.83

Notes: Column (1): spectral ID in LAMOST catalog. Col. (2): stellar subclass. Col. (3): Hα EWs. Col. (4): excess Hα EWs. Col. (5): Hα to bolometric flux ratio. Col. (6): corrected Hβ FWHMs. Col. (7): corrected Hα FWHMs. This entire table is available at `http://www.raa-journal.org/docs/Supp/ms4332Table3.txt`.

et al. (2013) derived $L_{\rm X}/L_{\rm bol} \propto (f_{\rm H\alpha}/f_{\rm bol})^{1.90\pm0.31}$. In our study, we have obtained that $f_{\rm X}/f_V \propto (f_{\rm H\alpha}/f_{\rm bol})^{1.12\pm0.30}$, a slightly flatter relation than those found in other studies. The discrepancy may be due to our small sample size. In addition, we should note that the lack of simultaneous observations for those two intrinsically varying properties (coronal and chromospheric activities) may introduce another source of uncertainty in all these studies (Martínez-Arnáiz et al. 2011).

4 THE BIMODALITY OF X-RAY ACTIVITY

The $\log(f_{\rm X}/f_V)$ distributions of G and K stars display clear bimodality (see Figs. 2 and 5). The gap between the peaks of the bimodal distribution is similar to that discovered by Vaughan & Preston (1980) using the Ca II H&K lines. That gap was first explained as a sudden change of dynamo activity to a less efficient mode at a critical rotation rate, but the scenario was rejected because the dependence of the chromospheric emission on rotation and spectral type is the same for stars above and below the gap (Noyes et al. 1984). Other studies with Ca II H&K, Hα and X-ray emission have also found the bimodality of stellar activity, with an active and inactive peak (e.g., Henry et al. 1996; Wright et al. 2004; Jenkins et al. 2011; Martínez-Arnáiz et al. 2011; Pace 2013). The bimodality is now explained as one young and one old subpopulation. The

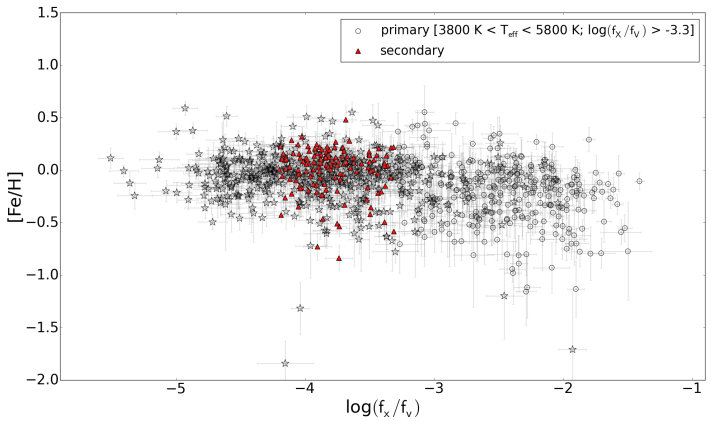

Fig. 7 Metallicity as a function of $\log(f_{\rm X}/f_V)$. The meanings of the symbols are the same as in Fig. 5.

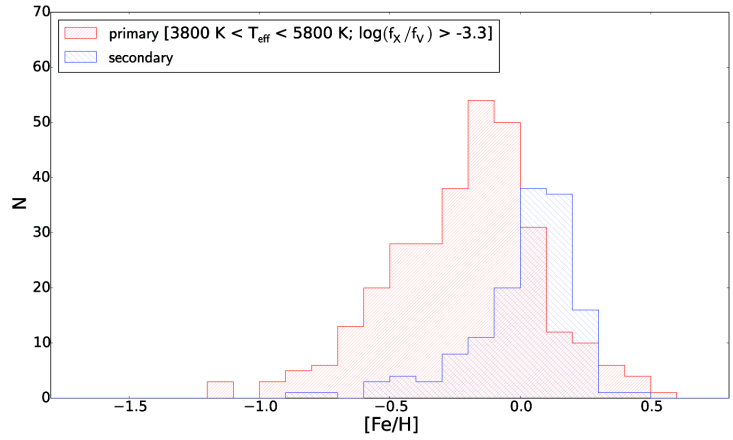

Fig. 8 Distribution of metallicities for stars in the primary and secondary branches.

old one is often thought to be inactive in chromospheric and X-ray emission, since the magnetic activity decreases simultaneously as the rotation decelerates with age (e.g., Mamajek & Hillenbrand 2008; Katsova & Livshits 2011).

The sky distribution (Fig. 13) shows no obvious distinction of the stars in the two branches. That means these two branches do not belong to different local structures (e.g., stellar streams). Before we discuss the bimodality of X-ray activity, we firstly checked the possibility that the bimodality is caused by selection effects, i.e., whether the detection limitations of *XMM-Newton* and LAMOST can produce a double-peaked distribution from a single-peaked $f_{\rm X}$ and a single-peaked V distribution.

4.1 Selection Effect

We performed a Monte Carlo simulation to check whether the bimodality is caused by selection effects. The detailed steps are as follows:

(i) We simulated a sample including 10 million sources with different effective temperatures, using the relative proportions from the LAMOST stellar parameter catalogs.

(ii) We obtained the relation between $\log(f_{\rm X}/f_V)$ and temperature by fitting to the observed distribution of the primary branch as

$$\begin{aligned}\log(f_{\rm X}/f_V) =&(-9.05\pm0.33)\times10^{-4}T\\&+(1.99\pm0.19)\,.\end{aligned}\tag{7}$$

With this equation, we calculated $\log(f_{\rm X}/f_V)$ values for the 10 million simulated sources.

(iii) We obtained the relation between absolute magnitude and temperature by fitting the data in Wegner (2007), using a cubic polynomial equation, as

$$\begin{aligned}M_V =&(-7.19\pm5.69)\times10^{-12}T^3\\&+(4.0\pm1.09)\times10^{-7}T^2\\&-(57.6\pm6.74)\times10^{-4}T+(25.5\pm1.32).\end{aligned}\tag{8}$$

Employing this equation, we calculated the absolute magnitudes for the simulated sources (Fig. 14, top-left panel).

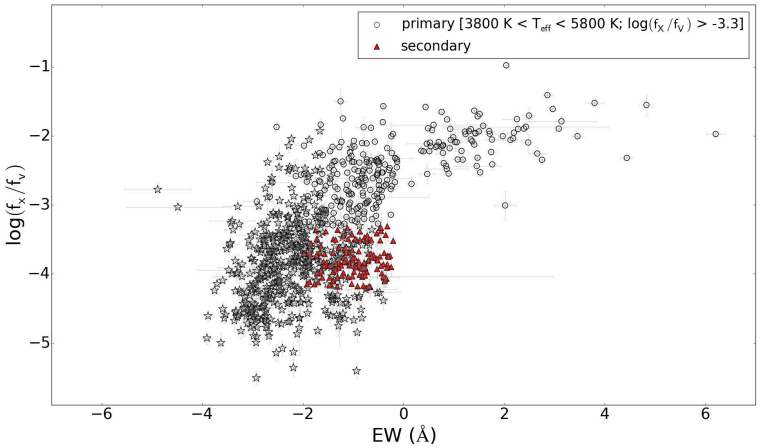

Fig. 9 $\log(f_{\rm X}/f_V)$ as a function of the EW of the Hα lines. The meanings of the symbols are the same as in Fig. 5.

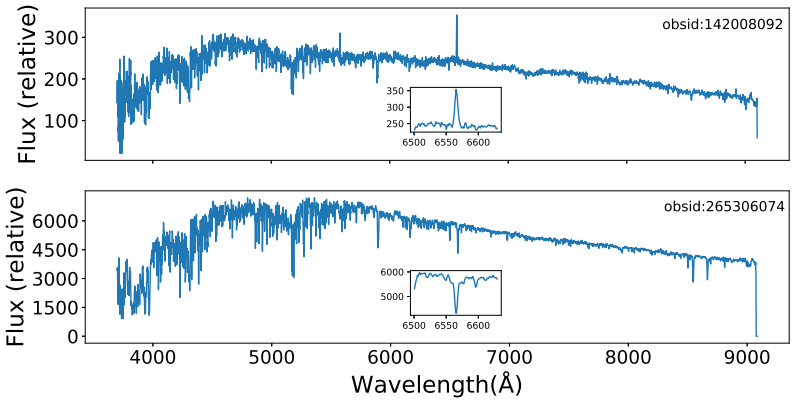

Fig. 10 Examples of LAMOST spectra for one active star (*top panel*) and one inactive star (*bottom panel*). The subplots feature the Hα lines.

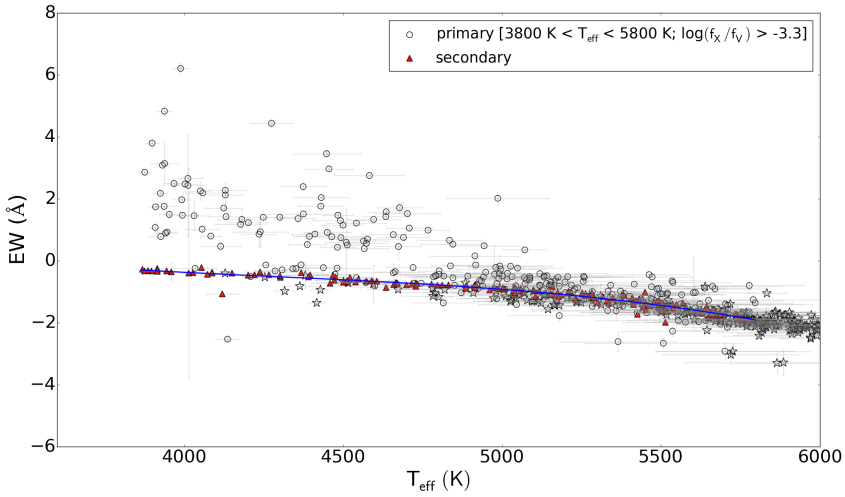

Fig. 11 EW$_{H\alpha}$ as a function of $T_{\rm eff}$. The meanings of the symbols are the same as in Fig. 5. The *solid line* is the fitted "base line" using the inactive stars in the secondary branch.

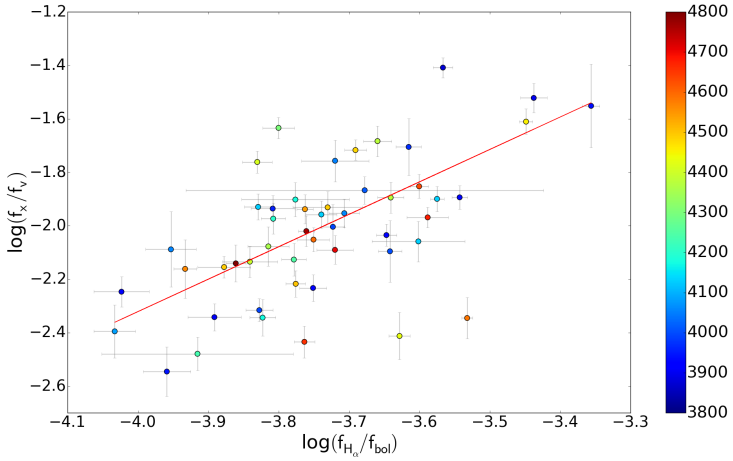

Fig. 12 $\log(f_{\rm X}/f_V)$ as a function of $\log(f_{\rm H\alpha}/f_{\rm bol})$. The color signifies different effective temperatures. The *red line* corresponds to the relationship $\log(f_{\rm X}/f_V) = (1.21 \pm 0.23) \times \log(f_{\rm H\alpha}/f_{\rm bol}) + (2.53 \pm 0.87)$.

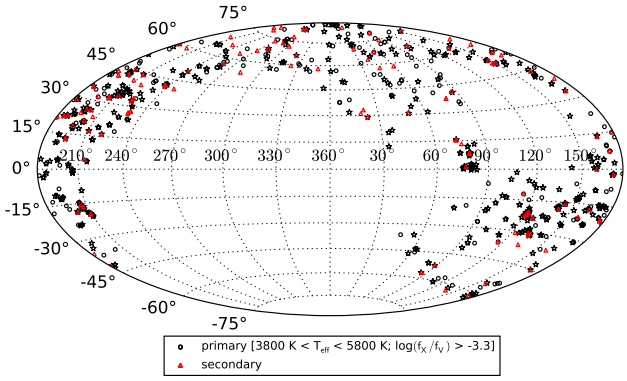

Fig. 13 The sky distribution of our stellar sources in Galactic coordinates. The meanings of the symbols are the same as in Fig. 5.

(iv) We derived the relation between X-ray luminosity and temperature by applying Equations (7) and (8), following,

$$\log(L_{\rm X}/L_V) = \log(f_{\rm X}/f_V), \quad (9)$$

and

$$\log(L_V) = -0.4 \times (M_V - M_{\odot,V}) - \log(L_{\odot,V}). \quad (10)$$

The absolute magnitude and luminosity for the Sun are 4.85 mag (Worthey et al. 1994) and 4.64×10^{32} erg s^{-1} [2] respectively. We then obtained the X-ray luminosities for the simulated stars (Fig. 14, bottom-left panel).

(v) Assuming the stars are located in the Galaxy, we assigned random distances (from 1 pc to 15 kpc; Amôres et al. 2017)) to each star (Fig. 14, top-right panel).

(vi) We calculated the apparent magnitude and X-ray flux using the simulated M_V and $L_{\rm X}$ respectively, and distance D. The detection limits were set for LAMOST ($10 < V < 20$) and *XMM-Newton* (10^{-15} erg s^{-1} $< f_{\rm X} <$ 10^{-11} erg s^{-1}) to select simulated sources that can be detected.

(vii) We re-calculated the $\log(f_{\rm X}/f_V)$ with Equation (3), using the apparent magnitude and X-ray flux. The simulated distribution is shown in Figure 14 (bottom-right panel).

The simulated distributions of M_V, $L_{\rm X}$ and $\log(f_{\rm X}/f_V)$ for G and K stars are plotted in Figure 15. The simulated single-peaked distributions of $\log(f_{\rm X}/f_V)$ mean that the observed bimodality of G and K stars (Fig. 2) is not due to the selection effect.

4.2 Hardness Ratio

The coronal temperature is known to be positively correlated with X-ray luminosity and stellar activity (e.g., Vaiana 1983; Schrijver et al. 1984; Schmitt 1997; Güdel

[2] *http://astro.pas.rochester.edu/~aquillen/ast142/costanti.html*

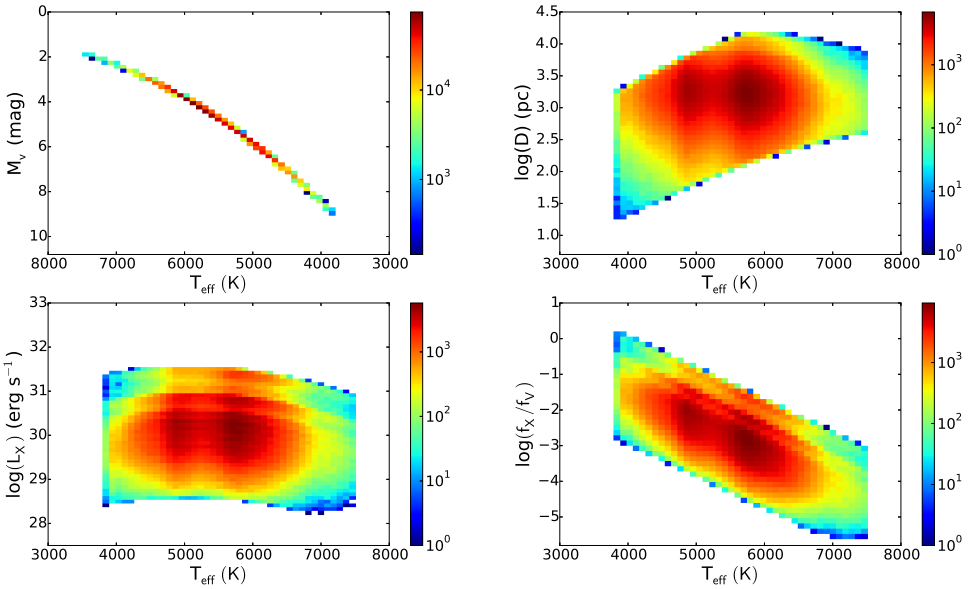

Fig. 14 Distributions of the parameters from the simulated sample. The color indicates the numbers of simulated sources. *Top-left panel*: absolute magnitude as a function of temperature for the simulated sources. *Bottom-left panel*: X-ray luminosity as a function of temperature for the simulated sources. *Top-right panel*: distance as a function of temperature for the simulated sources. *Bottom-right panel*: X-ray to optical flux ratio as a function of temperature for the simulated sources.

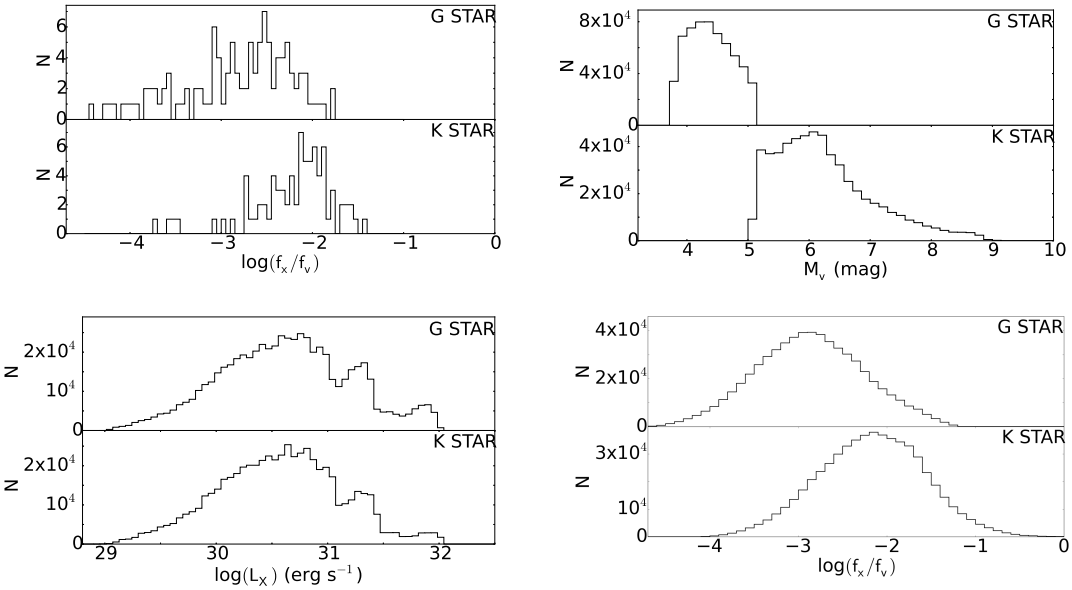

Fig. 15 Histograms of some parameters for G and K stars. *Top-left panel*: the observed $\log(f_{\rm X}/f_V)$ distributions of G and K stars in the primary branch. *Top-right panel*: the M_V distributions of the simulated G and K stars. *Bottom-left panel*: the $L_{\rm X}$ distributions of the simulated G and K stars. *Bottom-right panel*: the $\log(f_{\rm X}/f_V)$ distributions of the simulated G and K stars.

2004; Jeffries et al. 2006; Telleschi et al. 2005, 2007). The cause of this relation between coronal temperature and luminosity may be that they are both functions of magnetic activity (Güdel 2004). A more efficient dynamo inside active stars (for example because of faster rotation) produces stronger magnetic fields in the corona, and consequently a higher rate of field line reconnections and flares. This results both in a larger density of energetic electrons in the corona and in higher temperatures. Therefore, we suggest that the double-peaked distribution of $\log(f_{\rm X}/f_V)$ represents a double-peaked distribution of heating rates, and therefore coronal temperatures.

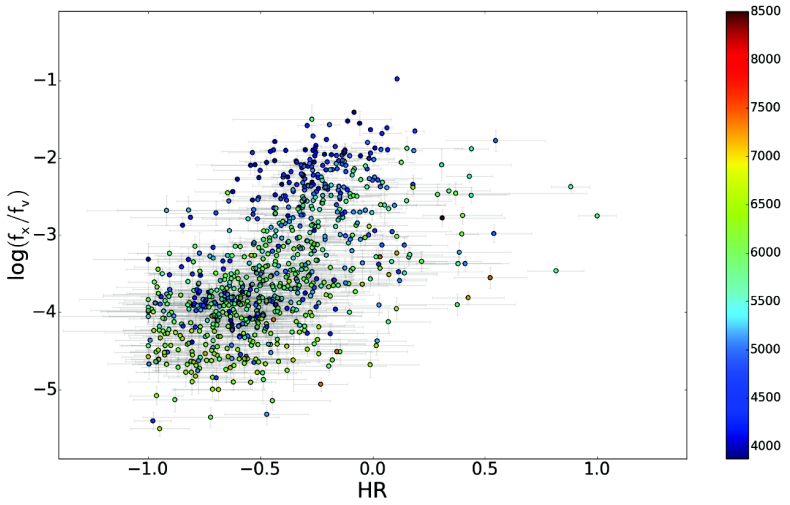

Fig. 16 $\log(f_{\rm X}/f_V)$ as a function of HR. The color signifies different effective temperatures.

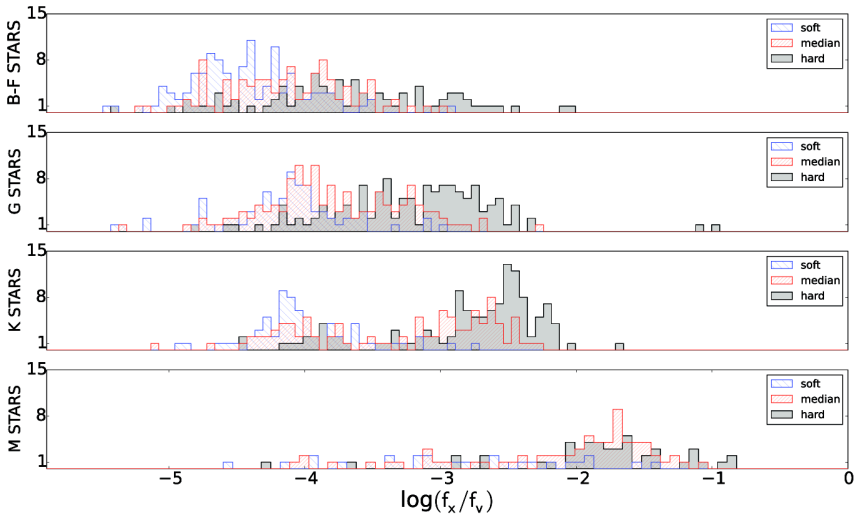

Fig. 17 Distribution of $\log(f_{\rm X}/f_V)$ for three types with different HR: hard ($0.3 < {\rm HR} < 1$), medium ($-0.6 < {\rm HR} < 0.3$) and soft ($-1 < {\rm HR} < -0.6$). It is clear that hard sources have the highest $\log(f_{\rm X}/f_V)$ values, while soft sources have the lowest values. The mean $\log(f_{\rm X}/f_V)$ values of the soft, medium and hard sources in G-type are -3.93, -3.48 and -2.81, and their standard deviations around the mean $\log(f_{\rm X}/f_V)$ are 0.53, 0.61 and 0.69, respectively. The mean $\log(f_{\rm X}/f_V)$ values of the three kinds of sources in the K-type are -3.75, -2.91 and -2.33, and their standard deviations around the mean $\log(f_{\rm X}/f_V)$ are 0.48, 0.8 and 0.67, respectively.

In our work, we take the X-ray HR as a proxy for the coronal temperature, because a hotter corona will emit photons with higher energies, which produces harder X-ray spectra. There is a positive correlation between $\log(f_{\rm X}/f_V)$ and HR (Fig. 16). That means stronger X-ray emitters (higher $\log(f_{\rm X}/f_V)$) have higher coronal temperatures. To more thoroughly investigate, we classified the objects into three types: hard, medium and soft sources, using the criteria as: hard ($0.3 < {\rm HR} < 1$), medium ($-0.6 < {\rm HR} < 0.3$) and soft ($-1 < {\rm HR} < -0.6$). We find (Fig. 17) that (1) the higher activity peak of the $\log(f_{\rm X}/f_V)$ distribution in G-type stars is dominated by hard sources, and the lower activity peak by medium and soft sources; (2) the higher activity peak of the $\log(f_{\rm X}/f_V)$ distribution in K-type stars is dominated by hard and medium sources, and the lower activity peak by soft sources.

Besides G and K stars, bimodality was also detected in late F and early M stars (Sect. 3.2), although the statistics are too poor due to the sample limit. One question is why the bimodality is not detected for those hotter or cooler stars. For hotter stars (early F and earlier), the coronal heating efficiency may be quite low for most of them. For cooler stars (late M), firstly, they are generally optically faint, thus our sample may be not complete; secondly, stars later than M4 type may have a different dynamo mech-

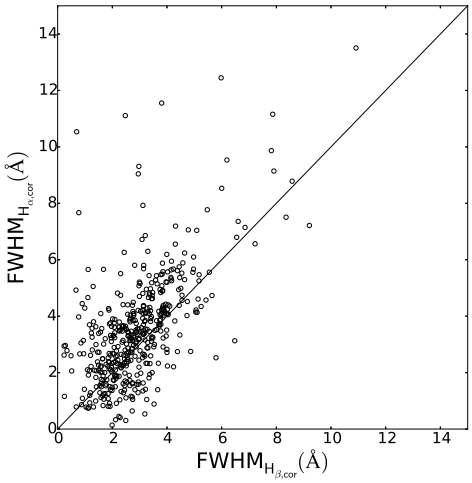

Fig. 18 Comparison of corrected FWHMs calculated from Hα and Hβ lines.

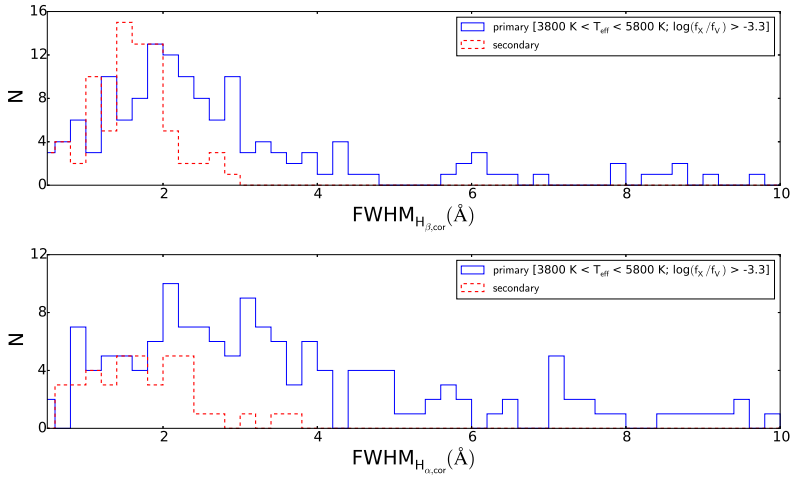

Fig. 19 *Top panel*: distributions of corrected FWHMs calculated from Hβ lines for the primary and secondary branch. *Bottom panel*: distributions of corrected FWHMs calculated from Hα lines for the primary and secondary branch.

anism due to their fully convective nature (Durney et al. 1993); thirdly, the evolution of M stars is very slow, which means most of them are still in the regime with a high coronal heating rate. In fact, most of the M stars have high HR values around 0 (Fig. 16).

4.3 Rotational Velocities

The magnetic dynamo suggests a lower rotation velocity for inactive stars than active ones. Therefore, we further checked the difference in rotational velocities for the primary branch ($3800\,\mathrm{K} < T_{\rm eff} < 5800\,\mathrm{K}$; $\log(f_{\rm X}/f_V) > -3.3$) and secondary branch. They can be regarded as the active and inactive parts (of G and K stars), respectively. In our work, we take the FWHMs of Balmer lines as proxies of rotational velocities (Strassmeier et al. 1990; Fekel 1997).

The instrumentally corrected FWHM is calculated as

$$\mathrm{FWHM_{cor}} = (\mathrm{FWHM_{obs}^2} - \mathrm{FWHM_{inst}^2})^{1/2}\ , \quad (11)$$

where $\mathrm{FWHM_{obs}}$ is the observed FWHM, $\mathrm{FWHM_{inst}}$ the FWHM of the lamp lines and $\mathrm{FWHM_{cor}}$ the corrected FWHM (Strassmeier et al. 1990). Here we calculated the FWHMs of Hα and Hβ lines for 540 and 596 stars, respectively (Table 3). Collisional broadening and broadening as a result of macro-turbulence were not corrected for. The corrected FWHMs measured from Hα and Hβ lines are in good agreement (Fig. 18). The mean deviation between the FWHMs from the two lines is ≈0.43 Å, with a standard deviation of ≈1.09 Å.

The FWHMs of the secondary branch stars are generally smaller than those of the primary branch stars (Fig. 19), indicating relatively lower rotational velocities of the secondary branch sources. This further explains the bimodality of the X-ray activity of G and K stars. Low rotational velocity weakens the coronal activity (Pallavicini et al. 1981; Pizzolato et al. 2003; Wright et al. 2011) and, therefore, the X-ray to optical flux ratio.

5 CONCLUSIONS

The *XMM-Newton* and LAMOST data allow us to identify X-ray emitters and probe stellar X-ray activity over a wide range of stellar parameters. By cross matching the 3XMM-DR5 catalog with the LAMOST DR3 catalog, we provide a sample including 1259 X-ray emitting stars, among which 1090 have accurate stellar parameter estimations. Our sample size is much larger than those in previous works.

We studied the X-ray emission level, using the X-ray to optical flux ratio, for different stellar types, including two B stars, 36 A stars, 317 F stars, 405 G stars, 332 K stars and 167 M stars. Late-type stars in general have higher $\log(f_{\rm X}/f_V)$ values than early-type ones, indicating their higher X-ray activity.

We find a bimodal distribution of $\log(f_{\rm X}/f_V)$ for G- and K-type stars. We performed a Monte Carlo simulation which demonstrates that the double-peaked distributions are not caused by a selection effect. We explain this bimodality as evidence of two subpopulations with different coronal heating rates, and therefore different coronal temperatures. Stars with a hotter corona — observationally with a higher HR — have a higher X-ray $\log(f_{\rm X}/f_V)$ value. Furthermore, we calculated the FWHMs of Hα and Hβ lines, and found that those inactive stars generally have smaller FWHMs, and therefore lower rotational velocities, than active stars. In fact, the $\log(f_{\rm X}/f_V)$ distributions of the late F and early M types also display weak bimodality, but the statistics are very poor due to the limited sample. Future studies with more F and M stars may shed more light on the distribution.

In general, the rotation velocity and stellar activity observationally decay with stellar age (e.g., Wilson 1963; Skumanich 1972; Simon et al. 1985; Cardini & Cassatella 2007; Mamajek & Hillenbrand 2008), therefore, those inactive stars with much higher $\log(g)$ values are possibly old stars. We speculate that the old age stellar activity cycles like those displayed by the Sun (Judge et al. 2003), and long-term variation (such as Maunder minimum: Baliunas & Jastrow 1990; Henry et al. 1996) may all contribute to the inactive part.

We also examined the correlation between $\log(f_{\rm X}/f_V)$ and Hα emission line luminosity and found a positive tight correlation between the two quantities.

Acknowledgements This research has made use of data obtained from the 3XMM XMM-Newton serendipitous source catalog compiled by the ten institutes of the XMM-Newton Survey Science Centre selected by ESA. The Guo Shou Jing Telescope (the Large Sky Area Multi-Object Fiber Spectroscopic Telescope, LAMOST) is a National Major Scientific Project built by the Chinese Academy of Sciences. Funding for the project has been provided by the National Development and Reform Commission. LAMOST is operated and managed by National Astronomical Observatories, Chinese Academy of Sciences. We acknowledge use of the SIMBAD database and the VizieR catalogue access tool, operated at CDS, Strasbourg, France, and of Astropy, a community-developed core Python package for Astronomy (Astropy Collaboration, 2013). We are grateful for support from the National Science Foundation of China (NSFC, Nos. 11273028, 11333004, 11603035, 11603038 and 11503054). RS acknowledges support from a Curtin University Senior Research Fellowship; he is also grateful for support, discussions and hospitality at the Strasbourg Observatory during part of this work.

References

Agüeros, M. A., Anderson, S. F., Covey, K. R., et al. 2009, ApJS, 181, 444
Amôres, E. B., Robin, A. C., & Reylé, C. 2017, A&A, 602, A67
Aurière, M., Konstantinova-Antova, R., Charbonnel, C., et al. 2015, A&A, 574, A90
Baliunas, S., & Jastrow, R. 1990, Nature, 348, 520
Brusa, M., Zamorani, G., Comastri, A., et al. 2007, ApJS, 172, 353
Cardini, D., & Cassatella, A. 2007, ApJ, 666, 393
Castelli, F., & Kurucz, R. L. 2004, astro-ph/0405087
Charbonneau, P. 2010, Living Reviews in Solar Physics, 7, 3
Ciardi, D. R., von Braun, K., Bryden, G., et al. 2011, AJ, 141, 108
Cui, X.-Q., Zhao, Y.-H., Chu, Y.-Q., et al. 2012, RAA (Research in Astronomy and Astrophysics), 12, 1197
Deng, L.-C., Newberg, H. J., Liu, C., et al. 2012, RAA (Research in Astronomy and Astrophysics), 12, 735
Durney, B. R., De Young, D. S., & Roxburgh, I. W. 1993, Sol. Phys., 145, 207
Fekel, F. C. 1997, PASP, 109, 514
Foight, D. R., Güver, T., Özel, F., & Slane, P. O. 2016, ApJ, 826, 66

Georgakakis, A., Georgantopoulos, I., Vallbé, M., et al. 2004, MNRAS, 349, 135
Güdel, M. 2004, A&A Rev., 12, 71
Harnden, Jr., F. R., Branduardi, G., Elvis, M., et al. 1979, ApJ, 234, L51
Henry, T. J., Soderblom, D. R., Donahue, R. A., & Baliunas, S. L. 1996, AJ, 111, 439
Hornschemeier, A. E., Bauer, F. E., Alexander, D. M., et al. 2003, AJ, 126, 575
Jardine, M., & Unruh, Y. C. 1999, A&A, 346, 883
Jeffries, R. D., Evans, P. A., Pye, J. P., & Briggs, K. R. 2006, MNRAS, 367, 781
Jenkins, J. S., Murgas, F., Rojo, P., et al. 2011, A&A, 531, A8
Jester, S., Schneider, D. P., Richards, G. T., et al. 2005, AJ, 130, 873
Judge, P. G., Solomon, S. C., & Ayres, T. R. 2003, ApJ, 593, 534
Katsova, M. M., & Livshits, M. A. 2011, Astronomy Reports, 55, 1123
Krautter, J., Zickgraf, F.-J., Appenzeller, I., et al. 1999, A&A, 350, 743
Lin, D., Webb, N. A., & Barret, D. 2012, ApJ, 756, 27
Luo, A.-L., Zhao, Y.-H., Zhao, G., et al. 2015, RAA (Research in Astronomy and Astrophysics), 15, 1095
Luo, B., Bauer, F. E., Brandt, W. N., et al. 2008, ApJS, 179, 19
Maccacaro, T., Gioia, I. M., Wolter, A., Zamorani, G., & Stocke, J. T. 1988, ApJ, 326, 680
Mamajek, E. E., & Hillenbrand, L. A. 2008, ApJ, 687, 1264
Martínez-Arnáiz, R., López-Santiago, J., Crespo-Chacón, I., & Montes, D. 2011, MNRAS, 414, 2629
Noyes, R. W., Hartmann, L. W., Baliunas, S. L., Duncan, D. K., & Vaughan, A. H. 1984, ApJ, 279, 763
Özdarcan, O., & Dal, H. A. 2018, Astronomische Nachrichten, 339, 277
Pace, G. 2013, A&A, 551, L8
Pallavicini, R., Golub, L., Rosner, R., et al. 1981, ApJ, 248, 279
Pizzolato, N., Maggio, A., Micela, G., Sciortino, S., & Ventura, P. 2003, A&A, 397, 147
Prosser, C. F., Randich, S., Stauffer, J. R., Schmitt, J. H. M. M., & Simon, T. 1996, AJ, 112, 1570
Reid, I. N., Hawley, S. L., & Gizis, J. E. 1995, AJ, 110, 1838
Reiners, A., Schüssler, M., & Passegger, V. M. 2014, ApJ, 794, 144
Rocha-Pinto, H. J., & Maciel, W. J. 1998, MNRAS, 298, 332
Rogel, A. B., Lugger, P. M., Cohn, H. N., et al. 2006, ApJS, 163, 160
Rosen, S. R., Webb, N. A., Watson, M. G., et al. 2016, A&A, 590, A1
Schlafly, E. F., & Finkbeiner, D. P. 2011, ApJ, 737, 103
Schmitt, J. H. M. M. 1997, A&A, 318, 215
Schmitt, J. H. M. M., Collura, A., Sciortino, S., et al. 1990, ApJ, 365, 704
Schmitt, J. H. M. M., Fleming, T. A., & Giampapa, M. S. 1995, ApJ, 450, 392
Schrijver, C. J., Mewe, R., & Walter, F. M. 1984, A&A, 138, 258
Schröder, C., & Schmitt, J. H. M. M. 2007, A&A, 475, 677
Simon, T., & Drake, S. A. 1989, ApJ, 346, 303
Simon, T., Herbig, G., & Boesgaard, A. M. 1985, ApJ, 293, 551
Skumanich, A. 1972, ApJ, 171, 565
Solanki, S. K., Motamen, S., & Keppens, R. 1997, A&A, 325, 1039
Stelzer, B., Marino, A., Micela, G., López-Santiago, J., & Liefke, C. 2013, MNRAS, 431, 2063
Stocke, J. T., Liebert, J., Gioia, I. M., et al. 1983, ApJ, 273, 458
Stocke, J. T., Morris, S. L., Gioia, I. M., et al. 1991, ApJS, 76, 813
Strassmeier, K. G., Fekel, F. C., Bopp, B. W., Dempsey, R. C., & Henry, G. W. 1990, ApJS, 72, 191
Telleschi, A., Güdel, M., Briggs, K., et al. 2005, ApJ, 622, 653
Telleschi, A., Güdel, M., Briggs, K. R., Audard, M., & Palla, F. 2007, A&A, 468, 425
Testa, P., Saar, S. H., & Drake, J. J. 2015, Philosophical Transactions of the Royal Society of London Series A, 373, 20140259
Vaiana, G. S. 1983, in IAU Symposium, 102, Solar and Stellar Magnetic Fields: Origins and Coronal Effects, ed. J. O. Stenflo, 165
Vaughan, A. H., & Preston, G. W. 1980, PASP, 92, 385
Vilhu, O. 1984, A&A, 133, 117
Vilhu, O., & Walter, F. M. 1987, ApJ, 321, 958
Voges, W., Aschenbach, B., Boller, T., et al. 1999, A&A, 349, 389
Walter, F. M., & Bowyer, S. 1981, ApJ, 245, 671
Wegner, W. 2007, MNRAS, 374, 1549
Wilson, O. C. 1963, ApJ, 138, 832
Worthey, G., Faber, S. M., Gonzalez, J. J., & Burstein, D. 1994, ApJS, 94, 687
Wright, J. T., Marcy, G. W., Butler, R. P., & Vogt, S. S. 2004, ApJS, 152, 261
Wright, N. J., Drake, J. J., Mamajek, E. E., & Henry, G. W. 2011, ApJ, 743, 48
Wu, Y., Luo, A.-L., Li, H.-N., et al. 2011, RAA (Research in Astronomy and Astrophysics), 11, 924
Xiang, M.-S., Liu, X.-W., Shi, J.-R., et al. 2017, MNRAS, 464, 3657
Yang, H., Liu, J., Gao, Q., et al. 2017, ApJ, 849, 36
Zacharias, N., Finch, C. T., Girard, T. M., et al. 2013, AJ, 145, 44
Zhao, G., Zhao, Y.-H., Chu, Y.-Q., et al. 2012, RAA (Research in Astronomy and Astrophysics), 12, 723
Zickgraf, F.-J., Engels, D., Hagen, H.-J., Reimers, D., & Voges, W. 2003, A&A, 406, 535